

# Fast Ion Confinement in Quasi-Axisymmetric Stellarator Equilibria

P. J. Bonofiglio<sup>1</sup>, D. W. Dudt<sup>2</sup>, C. P. S. Swanson<sup>2</sup>

<sup>1</sup>Princeton Plasma Physics Laboratory, Princeton, NJ 08543, USA

<sup>2</sup>Thea Energy, Princeton, NJ 08543, USA

E-mail: pbonofig@pppl.gov

20 December 2024

**Abstract.** This report presents an initial analysis of the fast ion confinement and losses within quasi-axisymmetric stellarator equilibria in consideration by Thea Energy. The equilibria have not yet been explicitly optimized for fast particle confinement and require validation. Modeling with the ASCOT5 code is used to directly examine the fast ion transport. The particle tracking simulations are purely (neo)classical in nature and simply contain the supplied equilibrium and collisions (pitch-angle, energy slowing, and velocity diffusion) from supplied thermal profiles. Uniform marker deposition is used to probe the general confinement properties of the equilibria while a realistic beam-born population is provided from the BEAMS3D code and an alpha particle population is calculated from a fusion source integrator. A first wall is included and defines the loss boundary. Analysis for NBI ions within Thea Energy's conceptual Eos neutron source are presented along with alpha particles in an enlarged DT-plasma. The fast ions are assessed in regards to their confinement time, pitch, energy, and spatial coordinates. For each population, the impact of collisions and orbit drifts are discussed. It is found that NBI born ions in Eos are strongly confined until slowing-down, owing largely to the tangential injection geometry, while 22% of DT-born alpha energy is lost in the scaled device, indicating that any fusion pilot plant design optimization should include metrics for fast ion confinement.

Submitted to: *Nucl. Fusion*

## 1. Introduction

The stellarator concept for magnetic confinement fusion has existed for decades. Unlike a tokamak, the stellarator confines plasma with purely external coils/magnets and is not axisymmetric. In a stellarator, the toroidal symmetry is broken as the plasma follows a helical structure with a specified periodicity. Traditionally, un-optimized stellarators exhibit very good stability but poor particle confinement. In particular, fast ion confinement drastically suffers due to the particle's fast velocity and large guiding-center drifts.

The toroidal symmetry breaking of the stellarator design creates magnetic wells in both the poloidal and toroidal directions. A particle with a sufficiently low pitch (here and hence after pitch is considered as  $v_{\parallel}/v$ ) may become trapped in the well, incurring periodic bouncing motion. This is the exact same physical mechanism as in a magnetic mirror [1, 2] or tokamak toroidal field ripple [3, 4, 5]. Consequently, the particles may not experience the full rotational transform and undergo cross-field guiding-center drifts which will produce large transport and losses [6]. Naturally, the strongest drifts in stellarators are the  $\nabla B$ , curvature, and  $\mathbf{E} \times \mathbf{B}$  (dependent on electric field strength [7]) drifts which are all proportional to the ion energy.

A great deal of research has taken place to minimize the cross-field guiding-center drifts and, thus, enhance particle confinement. This has led to the numerical construction of stellarator equilibria and the creation of omnigenity regimes [8]. In particular, a special subset of omnigenous geometries is quasi-symmetry in which magnetic contours are straight within the Boozer coordinate system [9, 10]. Quasi-symmetry can be further broken down by the defining symmetry: quasi-axisymmetry, quasi-helical symmetry, and quasi-poloidal symmetry. These stellarator classes are constructed such that the magnetic contours better follow the drift direction so that the radial drift motion averages to zero [11, 12, 13]. These improved confinement regimes have been experimentally verified in the quasihelically symmetric (HSX) device [14, 15] and quasi-isodynamic Wendelstein 7-X (W7-X) [16, 17].

There are many parameters to constrain and optimize for during the equilibrium construction. Since fast ions drifts are large, optimization schemes may include metrics to minimize the neoclassical and/or radial-drift transport of fast ions. Many schemes have been created and included within optimization loops, including: the minimization of magnetic wells for particle trapping [18], the constancy of the canonical momentum ( $P_{\phi}$ ) [19], minimization of orbit drift parameters [20], minimization of outward particle flux [21, 22], and full Monte-Carlo integration of

fast ion motion [23]. These methods have been effectively shown to reduce alpha particle losses to sub-tokamak levels [24, 25]. While integrating the fast ion trajectories is the only exact method for confirming the fast ion confinement, it is rather computationally expensive to calculate for each optimization loop and is, instead, often confirmed in a post-processing fashion [23]. This paper presents the latter case as no fast ion metric was included during the equilibrium optimization.

### 1.1. Thea Energy

Thea Energy is a private company focusing on stellarator design concepts for fusion energy. In particular, Thea Energy plans to employ a simplified system of planar coils [26]. This scheme will avoid the complex and difficult to engineer 3D magnetic coils that are commonly produced in traditional stellarator designs. This paper will present equilibria constructed from their proprietary coil system and the ensuing fast ion response.

Thea Energy is currently developing two stellarator machines: Eos and Helios. Eos is an intermediate design concept en route to a fusion reactor. Eos will act as a fusion neutron source from DD-interactions [27]. Eos will employ 10 MW of neutral beam injection (NBI) to drive the DD-fusion reactions. The beam injection is largely tangential and predominantly produces high pitch fast ions. Most of the neutrons will be sourced from beam-thermal reactions for tritium and other isotope production. Helios is the pilot plant concept which will focus on net energy production from DT-interactions with no beam heating.

Figure 1 shows a CAD rendering of the envisioned Eos device showing the toroidal field coils (white, orange, and dark blue), planar coils (small dark blue ovals), and NBI beamline (light blue). Further details

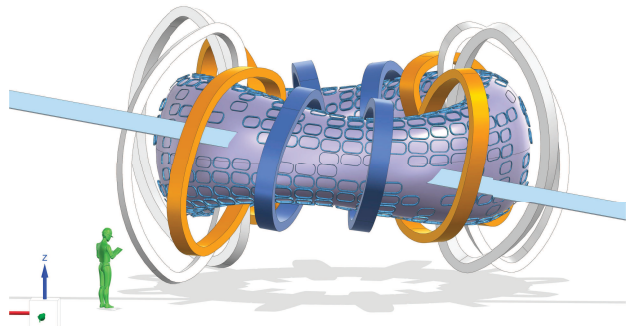


**Figure 1.** CAD rendering of the Eos device portraying the toroidal field coils (white, blue, and orange), neutral beam injection geometry (light blue), and planar coils (small blue ovals).

on the magnetic coil system may be found in [26]. One beam chord is imagined per field period (there are two field periods as discussed in the next section), and it is assumed that the optimal beam chord is tangent to the magnetic axis at the point on the axis where the

curvature is a minimum. For visualization purposes, the foregroundmost beamline is depicted in Figure 1. The additional beam properties are based on the 1 MeV ITER design [28].

Thea Energy has produced two-fold periodic quasi-axisymmetric equilibria from their realistic coil system for Eos. Their optimization scheme, however, does not yet directly account for the reduction of fast ion confinement. Hence, a direct verification of the fast ion confinement is needed at this stage of optimization. This paper presents the initial analysis of fast ion confinement in Thea Energy’s quasi-axisymmetric equilibria for Eos and a doubly-scaled Eos with DT-plasma. The analysis is performed with the ASCOT5 code [29] which takes the stellarator equilibria and fast ion population as input and calculates the resulting particle motion. ASCOT5 has been well benchmarked and verified against other particle-pushing codes and in stellarator scenarios [29, 30, 31]. Thermal profiles are optional input to calculate collisions with the background species. The confinement time and dependencies within velocity- and geometric-spaces are explored and presented for each respective fast ion population. The beam ion distribution is found with the BEAMS3D code [32] while fusion product distributions are found with a fusion source integrator [33] within ASCOT5.

The next section will briefly introduce the concept equilibria designed by Thea Energy for their Eos stellarator. Section 3 will discuss the general confinement properties from uniformly deposited particles which cover all of phase-space. Section 4 will go into detail on the confinement of beam-born ions and the resulting neutron flux in Eos, while Section 5 will present on the confinement of alpha particles in an enlarged Eos. The paper will conclude with a summary of the results, a brief discussion of their significance, and comments on future work.

## 2. Equilibrium Construction

Thea Energy is considering a quasi-axisymmetric design for both the Eos and Helios devices since this type of quasi-symmetry typically has a more compact geometry than other stellarators while serving as a proxy for particle confinement. While the design of quasi-axisymmetric equilibria has been around for decades [34, 35], more modern numerical approaches are being used that have shown exceedingly good fast particle confinement. A fixed-boundary equilibrium was optimized to have good quasi-axisymmetry, relatively high rotational transform and shear, moderate elongation, and a self-consistent bootstrap current [36]. No electric field was calculated or included in the equilibria design. This optimization was performed with the DESC code suite [37, 38] (note that DESC assumes nested flux surfaces), using

the “two-term” quasi-symmetry metric [39] and the bootstrap current formula from Redl et al. [40, 36]. A realizable set of planar coils was then found to reproduce this equilibrium with the FOCUS code [41, 26], and the free-boundary equilibrium corresponding to these coils was solved with DESC. This free-boundary equilibrium solution used a high enough numerical resolution to capture the toroidal field ripple from the smaller shaping coils. The Eos equilibrium has a major radius of  $R_0=3.24$  m, an aspect ratio of  $R_0/a=5.96$ , an average magnetic field strength on axis of  $|B|=5.00$  T, a volume-averaged normalized plasma pressure of  $\beta=2.54\%$ , and a vessel wall offset of 10 cm from the last closed flux surface (LCFS). A second, enlarged device and equilibrium was obtained by rescaling the dimensions of the Eos free-boundary solution by a factor of two, yielding a major radius of  $R_0=6.48$  m and a wall offset of 20 cm with the same aspect ratio and field strength. The bootstrap current is not necessarily self-consistent at this larger size since it depends on geometric factors, but the discrepancy was confirmed to be negligible.

The thermal profiles are shown in Figure 2 with the following functional forms:

$$n = 2.0 \times 10^{20} (1 - \rho^2)^{2/3} [\text{m}^{-3}] \quad (1)$$

$$T = 8.0 \times 10^3 (1 - \rho^2)^{1/3} [\text{eV}] \quad (2)$$

where  $\rho$  is the root-normalized toroidal flux,  $\rho = \sqrt{\psi_t/\psi_t(a)}$ . Since the two equilibria only differ by a linear scaling, the thermal profiles are identical between the two devices. The electron and ion components were assumed to be equal so that  $n_e = n_i$  and  $T_e = T_i$ . The profiles for Eos and Helios are still

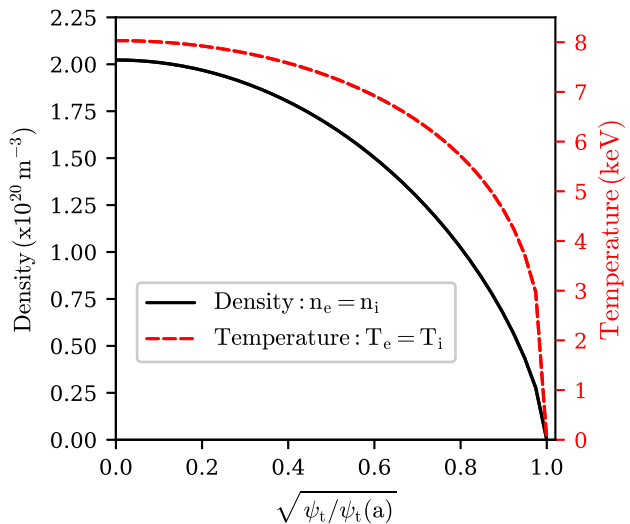


**Figure 2.** Thermal density and temperature profiles. Note that  $n_e = n_i$  and  $T_e = T_i$ .

being finalized, but more information regarding the Eos operating point is given in Swanson et al. [27], who find

that a less dense, hotter operating point with a hot-electron mode is advantageous for tritium production in Eos (this is also briefly analyzed in Section 4.3). A higher operating temperature is also envisioned for Helios. The presented work is not intended to prescribe profiles; rather it uses generally plausible profiles for the purpose of specificity and to compare results among models in regards to fast ion confinement.

The equilibria are depicted in Figures 3 and 4. Figure 3 presents the corresponding magnetic axis, LCFS, and wall for both Eos and the enlarged Eos over one field period. Please note the different axis

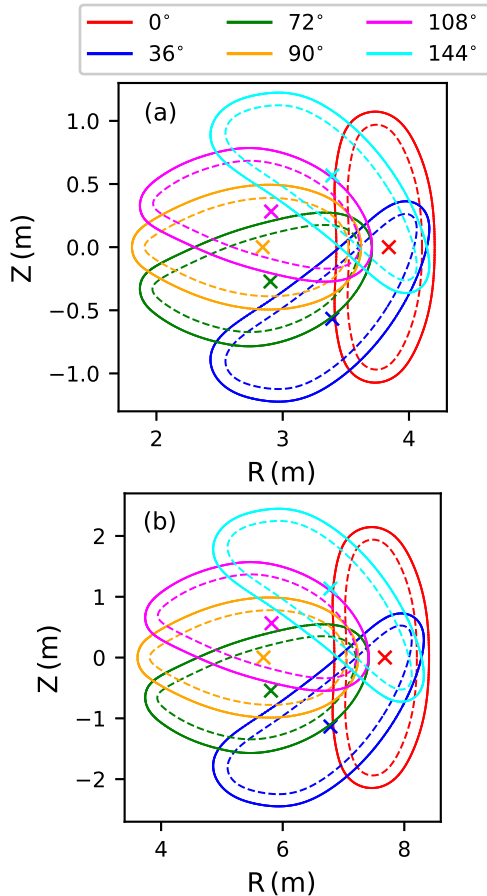


**Figure 3.** Last closed flux surfaces for the Eos, (a), and doubly-scaled Eos, (b), equilibria as a function of toroidal angle. Solid = wall and dashed = LCFS. The X's denote the locations of the magnetic axes. The poloidal angle is counter-clockwise within each respective surface. Note the different R and Z values.

scales in Figure 3. No magnetic islands or fast ion pressures/currents are included in the equilibria reconstructions. The assessment of additional magnetohydrodynamic (MHD) and kinetic fast ion effects on the equilibria are left for future work. Subfigure (a) of Figure 4 displays the rotational transform profile while subplots (b) and (c) present the magnetic contours at  $\rho=0.3$  and  $\rho=0.8$ , respectively. For reference, a magnetic field line is overplotted in Figure 4 as a solid black line. The horizontal magnetic contours in Boozer coordinates are qualitatively close to quasi-axisymmetry, and the largest symmetry-breaking component of the magnetic field on any surface for both equilibria is about 0.01 T. This level of quasi-symmetry is expected to naturally reduce the amount of outward drift transport, but this must be validated since the fast ion losses were not directly considered in the optimization. As such, the following sections are dedicated to analyzing fast ion trajectories within the Eos and enlarged Eos conceptual equilibria.

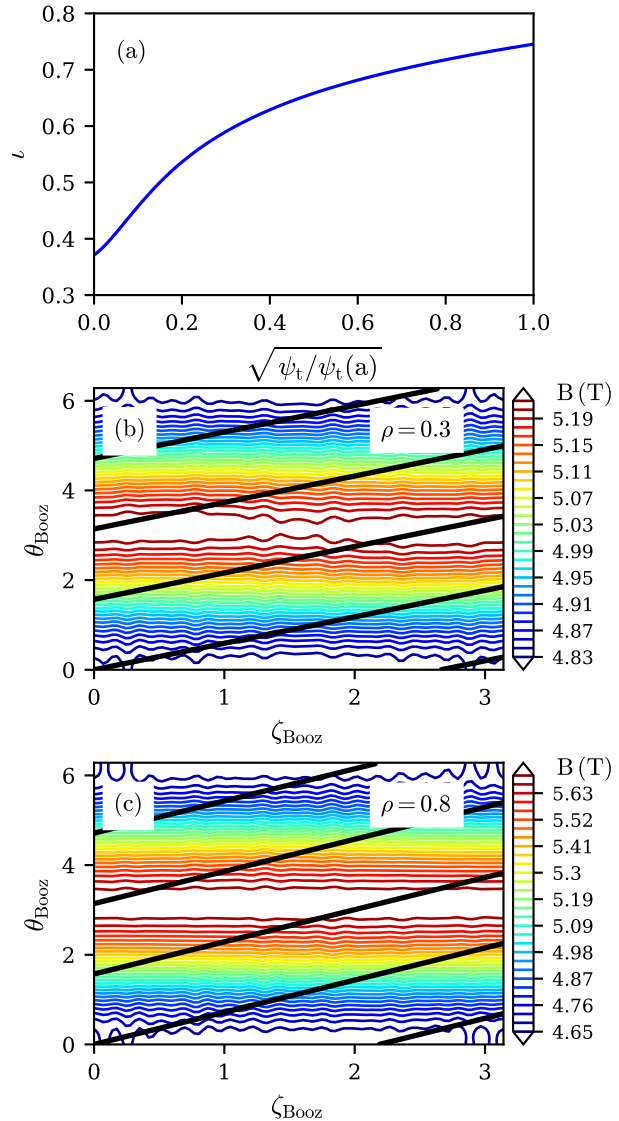


**Figure 4.** Iota for the Eos equilibrium, (a). The magnetic contours at  $\rho=\sqrt{\psi_t/\psi_t(a)}=0.3$ , (b), and  $\rho=0.8$ , (c). A magnetic fieldline is overplotted in black for both contours.

coordinates are qualitatively close to quasi-axisymmetry, and the largest symmetry-breaking component of the magnetic field on any surface for both equilibria is about 0.01 T. This level of quasi-symmetry is expected to naturally reduce the amount of outward drift transport, but this must be validated since the fast ion losses were not directly considered in the optimization. As such, the following sections are dedicated to analyzing fast ion trajectories within the Eos and enlarged Eos conceptual equilibria.

### 3. General Confinement

To probe the general confinement of fast ions, deuterium markers were deposited in the Eos concept equilibrium. In doing so, markers were sampled uniformly for analysis. The marker energies were chosen from 800-1100 keV to mimic beam-born ions

(discussed in the next section), and pitches spanned the full range of -1 to 1. In regards to geometric deposition, the markers were sampled with a random toroidal position, and the corresponding (R,Z) locations were chosen within the LCFS at the given toroidal angle. Thus, the initial sampling is uniform within  $(R, \phi, Z)$ . Since the markers have no connection to a physical source, the marker weights are all unity with no units.

100,000 markers were simulated for 10 ms without collisions in a guiding-center fashion, and the LCFS was taken as the loss boundary. At  $\sim 1$  MeV energies, 10 ms should produce a sufficient number of poloidal and toroidal transits to demonstrate trapped-orbit effects and general, overall, confinement. Examples of confined orbits are shown in Figure 5 for 1 MeV deuterons in the Eos candidate equilibrium for 0.8 ms. Subplot (a) shows a toroidal banana orbit (initial

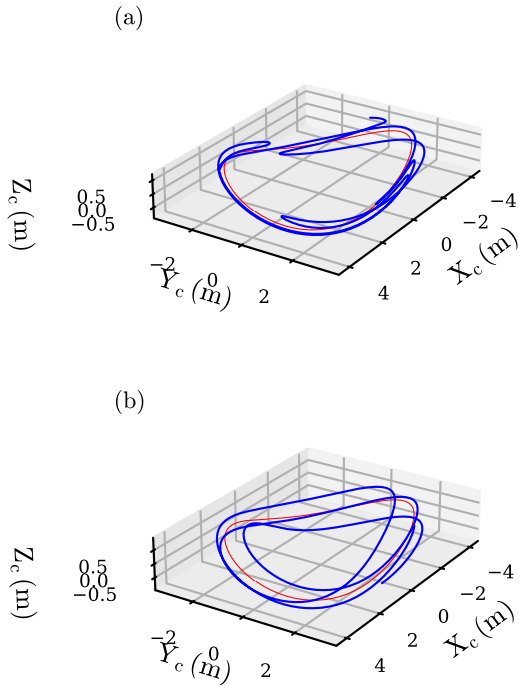


**Figure 5.** Examples of a confined toroidally trapped orbit, (a), and a confined co-passing orbit, (b), within the Eos concept equilibrium. The magnetic axis is plotted in red for reference.

pitch of 0.1; initial  $\sqrt{\psi_t/\psi_t(a)}=0.3$ ) while subplot (b) demonstrates a co-passing orbit (initial pitch of 0.95; initial  $\sqrt{\psi_t/\psi_t(a)}=0.75$ ).

The uniform deuteron distribution in the Eos concept equilibrium produced the loss histogram shown in Figure 6. The inset figure zooms in to make the long loss time tail more visible. It is immediately apparent that the overwhelming majority of losses occur within the first time bin. These are prompt losses where the marker is born very near the edge and its drift surface/banana width takes it over the

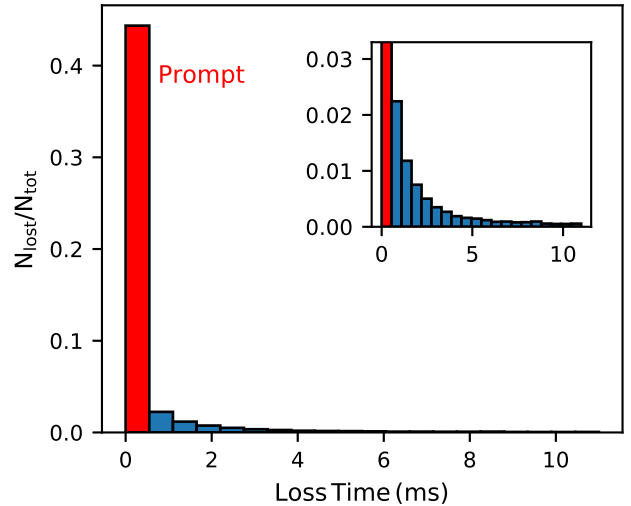


**Figure 6.** Histogram of losses as a function of loss time for uniformly deposited markers. The inset figure zooms in to eliminate prompt losses from view.  $N_{\text{lost}}/N_{\text{tot}}$  is the total number of particles. The red bar denotes the region of dominant prompt losses.

LCFS within a poloidal/banana transit. These values have been explicitly labeled for clarity. Excluding these markers results in a loss fraction of  $9.6\% \pm 1.0\%$ , which can be attributed to orbit drifts. The uncertainties follow from Monte-Carlo counting statistics where the uncertainty,  $\sigma$ , is calculated as  $\sigma = \sqrt{\bar{x}/N}$ , where  $\bar{x}$  is the measurement (loss fraction in this case) and  $N$  is the total number of markers. Naturally, the error reduces as the marker count increases.

This is unsurprising for a uniform distribution where markers may be sampled near the LCFS. This is apparent in Figure 7 subplot (a) which shows the loss fraction as a function of the marker's initial root-normalized toroidal flux. Figure 7 (a) shows that losses are dominant near the plasma edge then quickly decay as the marker position is more core-localized. This is consistent with expectations as the more core-deposited markers require longer drift times to be lost and, thus, experience stronger confinement. Figure 8 subplot (a) visualizes this by plotting the loss times against the initial radial position. Again, the prompt losses are evident for particles near the LCFS while core-localized particles experience weak losses and are close to perfectly confined beyond 5 ms.

Subplots (b) and (c) of Figure 7 present the loss fraction as a function of the final poloidal and toroidal angles, respectively, while subplot (d) displays the losses as a function of final energy and pitch. The distribution in poloidal angle is skewed to the top-half of the machine ( $0^\circ$  denotes the outboard midplane with positive values moving counter-clockwise). This is due to the  $\nabla B$  and curvature drifts, which are vertical. Recall that there is no electric field in our calculations and, thus, no  $\mathbf{E} \times \mathbf{B}$  drift. Particles that are lost due to drift-orbits simply undergo upward

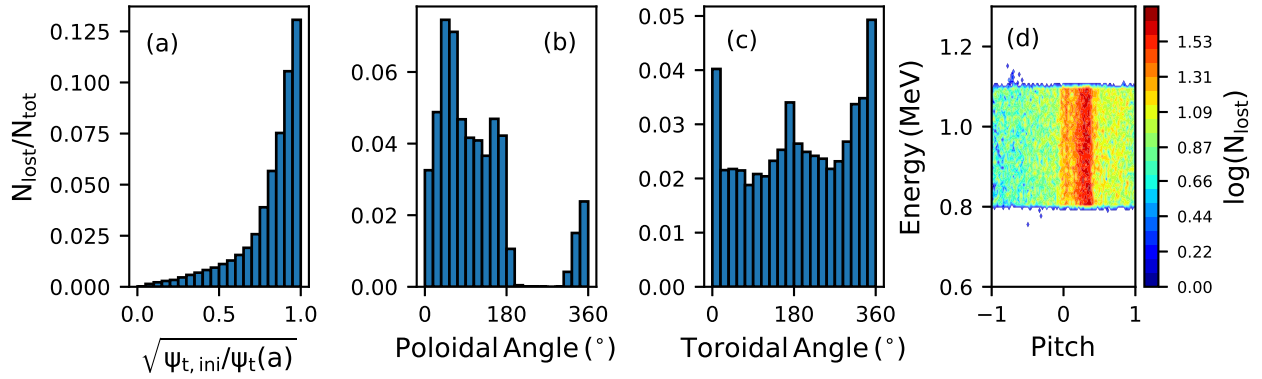


**Figure 7.** Histograms of losses for uniformly deposited markers as a function of initial radial position, (a), final poloidal angle, (b), final toroidal angle, (c), and final (energy,pitch)-space, (d).

deflection of their drift surfaces until they are lost. This was numerically confirmed by repeating the simulation and changing the particle charge to negative. The resulting poloidal distribution was inverted and losses were observed on the bottom-half of the machine. The toroidal deposition is somewhat uniform but appears to have a two-fold periodicity which is consistent with the two-fold symmetry of the quasi-axisymmetric equilibrium. Lastly, a slight preference to positive pitch is observed which simply correlates to trapped orbits on the inward swing of their banana orbits.

The (energy,pitch) loss distribution is more revealing in pitch-space. While there is no observed dependence on energy, the losses are dominant at low pitch values near 0. These correspond to deeply trapped orbits which should experience outward radial drift transport. Figure 8 subplot (b) demonstrates the losses as a function of radius and pitch and clearly highlights the preferential losses at low pitch. Close to the core, only markers with pitch near 0 are lost while the sensitivity to pitch broadens with increasing radius. This is the loss cone in velocity-space that defines lost orbits due to trapped orbit effects [42]. The cone is predominantly composed of trapped/banana orbits (see Figure 9 as an example), but dictates the regions in velocity-space of any orbit that drifts out. Core confinement is very good and requires very low pitch for the magnetic well trapping and drift transport. The loss cone is slightly shifted from zero pitch due to the recording of particle pitch relative to the turning points. Depending on which leg of the banana orbit the particle lies, the pitch will shift to slightly positive or negative. Again, Figure 8 shows that the losses are dominated by prompt orbits near the edge. Subplot (b) shows that edge orbits are lost regardless of pitch, and subplot (a) shows the edge losses occur almost instantly. The core and mid-radius ions are nearly perfectly confined after 5 ms and require very low pitch.

An example of a lost orbit is shown in Figure 9. Subplot (a) shows the poloidal motion in the  $(\rho, \theta_B)$ -coordinate system where  $\theta_B$  is the poloidal Boozer angle, while subplot (b) displays the radial coordinate

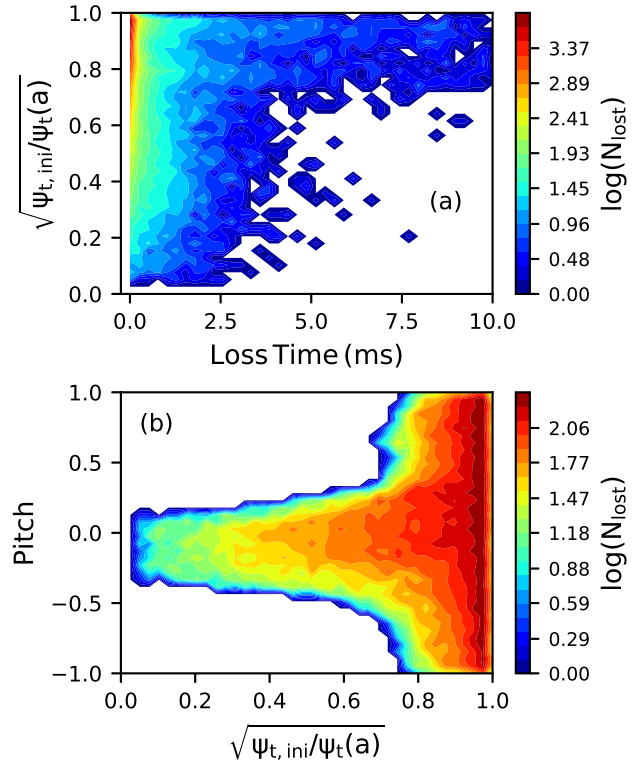


**Figure 8.** 2D-histograms of losses for uniformly deposited markers as a function of loss time and initial radial location, (a), and initial radial position and pitch, (b), displaying the loss cone.

as a function of time, and subplot (c) is a view of the motion from above. The bounce points are denoted by the green-to-yellow markers. Figure 9 shows wide banana orbits that undergo diffusive-drift motion outward [25]. It was found that this motion and loss mechanism were characteristic for all notable losses at low-pitch. In general, Figure 9 serves as an example to highlight the dominant orbit loss mechanism due to the equilibrium and re-emphasize how low-pitch ions are the most susceptible.

Overall, the uniform distribution of fast ion markers in the Eos concept equilibrium are consistent with expectations. The losses and distributions follow standard stellarator transport theory. While the

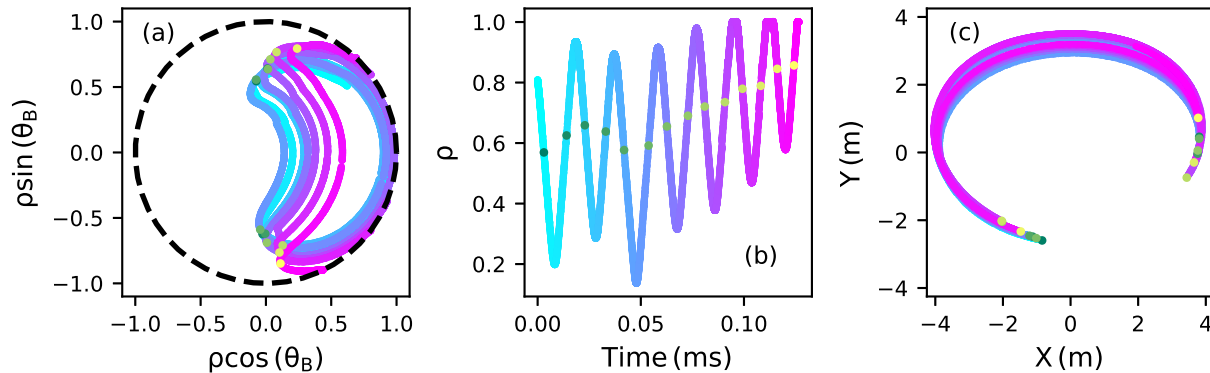


**Figure 9.** An example lost orbit from diffusive banana motion. The poloidal motion as a function of the generalized radial coordinate ( $\rho = \sqrt{\psi_t/\psi_t(a)}$ ) and poloidal Boozer angle ( $\theta_B$ ), (a), the radial coordinate as a function of time, (b), and the motion of the orbit in the toroidal plane as viewed from above, (c). The bounce points are marked by the points that transition from green to yellow with time, while the orbit changes from blue to pink in time.

prompt losses are excessive, orbit and drift effects give rise to a much lower loss fraction. The next section is dedicated to the much more physical scenario of NBI born ions with realistic deposition and slowing-down.

#### 4. Beam-born Confinement in Eos

Preliminary lines of sight were determined for neutral beam injection on the Eos device. Based on ITER neutral beam designs [28], two tangential neutral beams each injecting 5 MW of 1 MeV deuterons are considered for fast ion analysis. It should be noted that the beams inject opposite to one another such that one is in the + toroidal direction and the other in the - toroidal direction. This setup should drive minimal rotation and flow. Any beam supplied current, rotation, or electric field has not been calculated and omitted from the simulations. The BEAMS3D code [32] was used to determine the initial beam depositions from the beam geometry, magnetic equilibrium, and thermal profiles. A summary of the deposition properties is shown in Figure 10.

The deposition is slightly off-axis with a peak near  $\sqrt{\psi_t/\psi_t(a)}=0.2$  and is highly localized in the toroidal and poloidal angles due to the injection locations. The deposition is predominantly at the mid-plane ( $\theta=0^\circ=360^\circ$ ) and toroidally localized around  $117^\circ$  and  $243^\circ$ . Seen in subplots (c) and (d), the deposition energy is sharply peaked around the 1 MeV injection energy, and the pitch is highly concentrated at  $\pm 1$ . The  $\pm 1$  pitch correlates to the co- and counter-tangential injection. For reference, the slowed, steady-state, distribution is also plotted in Figure 10 (c) as found from ASCOT5 (blue histogram) and from analytic theory (green line) [43].

The density and temperature profiles are identical for thermal ions and electrons with a core peak density and temperature of  $2 \times 10^{20} m^{-3}$  and 8 keV, respectively, see Figure 2. For reference, the slowing-down time for a core-deposited 1 MeV deuteron in Eos is about 260 ms. The ASCOT5 steady-state

distribution was found by following the deposited markers for over a full slowing-down time and histogramming the distribution throughout the run (same procedure as in [29] and [31]). All collisions (pitch-angle, energy-slowing, and momentum diffusion) were included in all fast ion transport simulations in Sections 4 and 5 unless specifically noted.

100,000 markers were sampled from the BEAMS3D computed NBI deposition and followed until thermalization or lost to the wall. The particle motion was treated in a guiding-center fashion until the markers reached  $\sqrt{\psi_t/\psi_t(a)}=0.8$  at which point the full orbit motion was calculated. The gyrophase is tracked from initialization, which was random, so that when a marker hits the defined boundary ( $\rho = 0.8$ ), the full orbit motion picks up at the tabulated gyrophase and continues at the same phasing/orbit helicity. The inverse holds if the marker transitions back across the boundary. This allows for a more accurate loss deposition while being more computationally efficient. Marker weights were appended to each particle proportional to the ion source rate (#/s), giving the results more physical significance. The fraction of lost particles as a function of time is shown in Figure 11. Compared to the uniform deposition case, the overall loss fraction has dropped to about  $22.1\% \pm 1.5\%$ , of which 10.4% were lost after slowing and 4.2% were near-edge particles who are lost within a poloidal transit to the wall. Again, the largest number of losses is present from prompt loss orbits that are born near the LCFS along the beam deposition line of sight. These are the markers to the far right in Figure 10 (a) and account for about 4% of the total losses. Otherwise, a new loss feature in time is observed that peaks around 250 ms.

Examining Figure 12 (a), one can see that the loss time is clearly linked to the particle energy. The dashed black line represents the exponential decay calculated from theory for a 1 MeV deuteron with a 260 ms slowing-down time. Note that the loss fraction

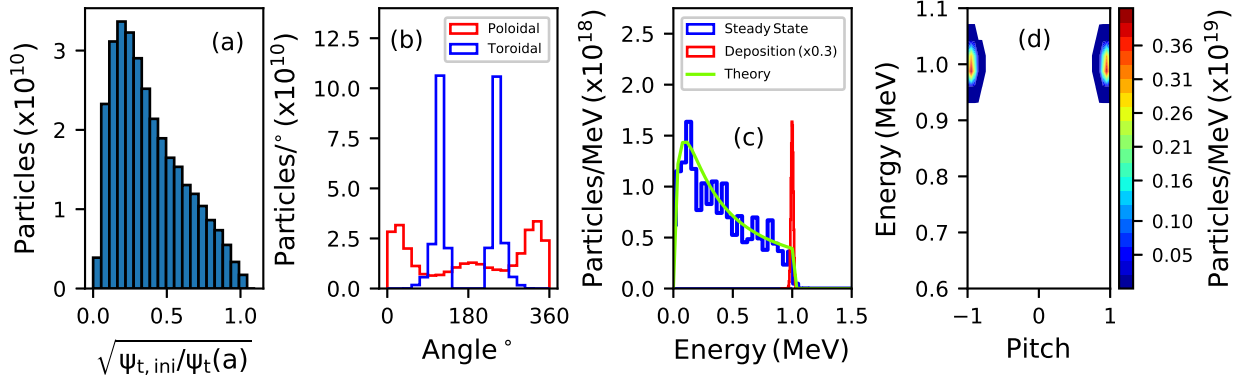


**Figure 10.** Neutral beam deposition as a function of root-normalized toroidal flux, (a), poloidal and toroidal angles, (b), energy, (c), and (energy,pitch)-space, (d). For reference, the slowed distribution in energy-space is also shown in subplot (c) as calculated from ASCOT5 and analytic theory.

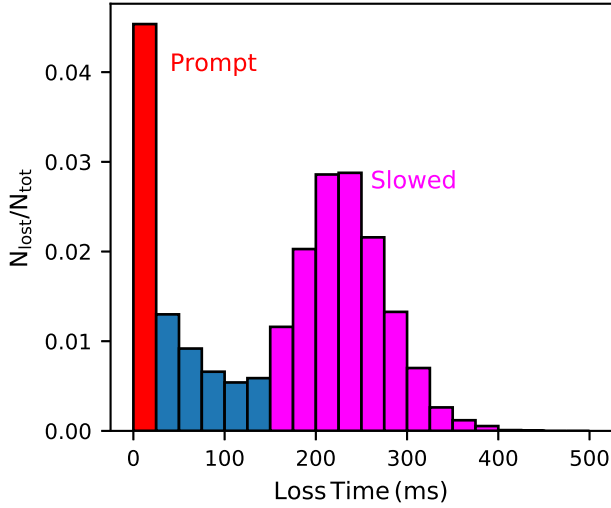


**Figure 11.** Histogram of the fraction of losses as a function of time for NBI deposited markers. The red bar denotes the region of dominant prompt losses and the magenta region denotes the region of slowed particles.

is plotted on a log scale since the points near 1 MeV and  $t=0$  dominate. These are the prompt losses strongly seen in Figure 11. Two loss populations are present and have been labeled with the same color as in Figure 11. A loss feature near the injection energy of 1 MeV and simulation start, and a larger, but weaker, distribution centered at 250 ms and low energy (sub 200 keV). The second loss feature corresponds to slowed, or near-slowed, losses. The distribution is centered right at the beam slowing-down time where higher loss times correspond to collisional slowing farther out in radius as the thermal profiles decrease in temperature.

For comparison, subplots (b) and (c) repeated the simulation with only energy slowing collisions (subplot (b)) and with no collisions (subplot (c)). While the simulation with energy slowing shows continual losses as the ions slow, similar to subplot (a), the region of enhanced losses near  $t=250$  ms are greatly reduced (recall the log-scale). This clearly shows that the additional pitch-angle collisions are important and

drive the ‘slowed’ loss region in subplot (a). As the beam ions slow, their collisionality increases, allowing for enhanced well-trapping and drift banana transport. This is clear in Figure 13 as well.

The radial dependence as a function of loss time is visualized in Figure 13 where the particles’ initial radial coordinate is plotted against their loss times. The two loss populations (prompt and slowed) are, again, plainly evident in subplot (a). The prompt losses occur at the simulation start at root-normalized toroidal flux greater than 0.8, while the slowed population is present near 250 ms and later at more inward radii. As the particles slow, we begin to see losses at the mid- to core-radii after about 150 ms at which point the particles become sub 300 keV (see Figure 12). As the ions approach thermalization at 250 ms, the losses become prominent at all radii up to 0.8 as pitch-angle collisions take over. For times greater than 250 ms, the losses are skewed to higher radii. This is consistent with the thermal density roll off and an increased collision time. For reference, the critical energy is about 150 keV, so the 1 MeV deuterons will almost fully slow on the electrons, of which the collisional slowing occurs faster than the pitch-angle collisions. When the beam ions slow to sub 400 keV, scattering from thermal ions begins to grow and drive additional transport. Furthermore, subplot (b), shows that core to mid-radius beam ions are perfectly confined when ignoring pitch-angle scattering and confirms that collisions are necessary in Eos to drive core-confined beam losses.

Figure 14 serves as a final summary figure and encompasses the observations previously noted. In short, the beam ions only exhibit two loss populations: prompt losses and nearly slowed ions. The former group could be reduced with alterations in beam geometry and location. Interestingly, from subplot (d), it can be seen that the co-injected beam experiences less prompt loss than the counter-injected beam, which implies that the co-injection geometry is slightly better. Additionally, lowering the beam divergence,

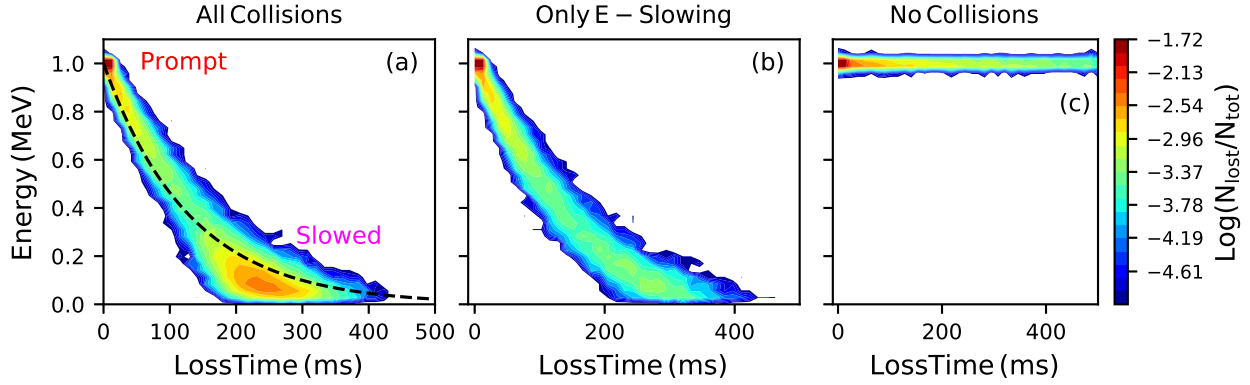


**Figure 12.** NBI born loss fraction as a function of the particle energy and loss time for simulations including all forms of collisions, (a), only energy slowing collisions, (b), and no collisions, (c). The dashed black line in (a) is the exponential energy decay from theory for a 1 MeV deuteron with a slowing time of 260 ms.

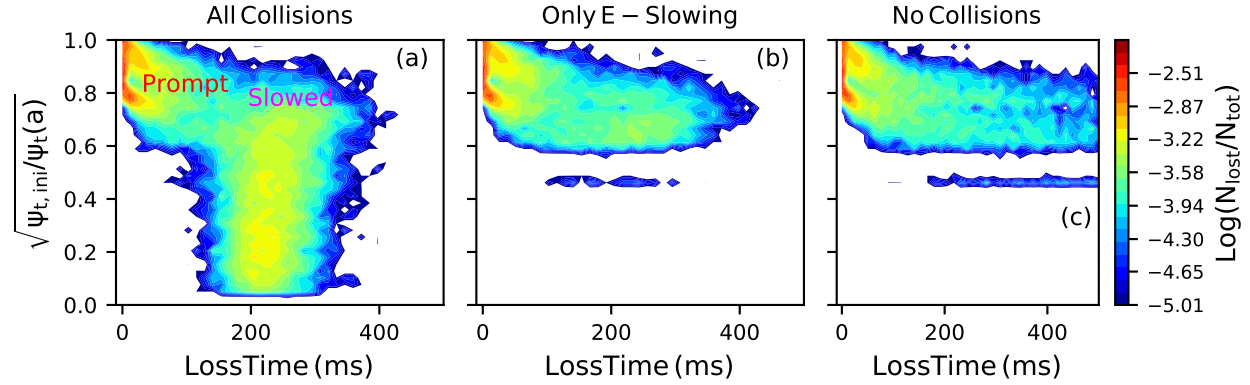


**Figure 13.** NBI born loss fraction as a function of the initial particle radii (root-normalized toroidal flux) and loss time for simulations including all forms of collisions, (a), only energy slowing collisions, (b), and no collisions, (c).

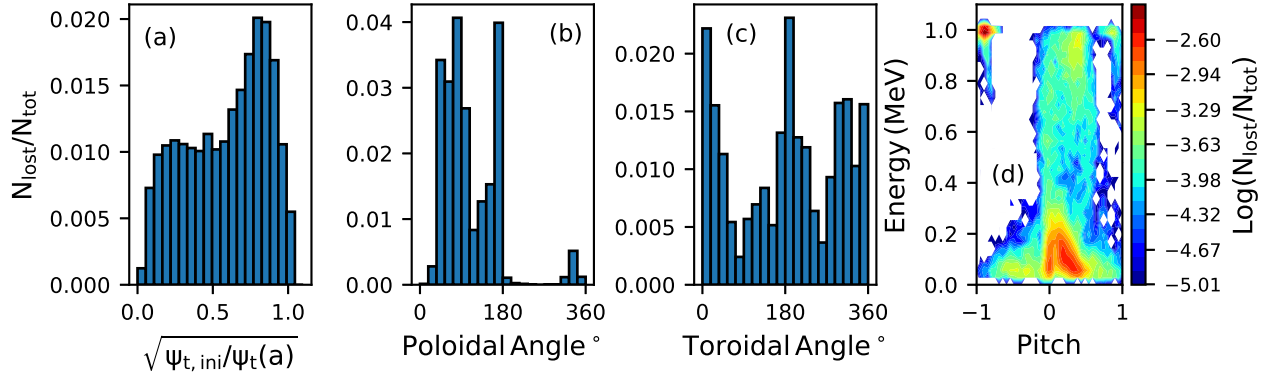


**Figure 14.** NBI born losses as a function of initial root-normalized toroidal flux, (a), final poloidal angle, (b), final toroidal angle, (c), and final (energy,pitch)-space, (d).

focusing on closer core-deposition, and potentially a new toroidal injection location could also mitigate prompt losses. The second loss population of nearly slowed ions is actually not too much of a concern. The whole purpose of the beam-born ions is to heat the plasma through collisional slowing and drive DD-fusion reactions. If beam-born ions are confined until nearly slowed, then they are doing their job of heating the plasma and potentially fusing via beam-thermal interactions. Discarding the sufficiently slowed ions ( $E < 200$  keV), the loss fraction is  $10.4\% \pm 1.0\%$ .

Subplot (a) demonstrates that the strongest losses

occur at high radius, and subplot (b) shows that the losses are again dominant on the top-half of the machine due to drifts. Subplot (c) presents the toroidal deposition of losses which seem to be consistent with the two-fold periodicity observed in Figure 7 (c). Lastly, subplot (d), again, presents the high-energy prompt losses and slowed losses. It is apparent that the slowed losses occur at low values of pitch, consistent with the loss condition of Figure 8 and pitch-angle scattering.

Figure 15 shows the wall heat load produced from the lost beam ions in Eos. The wall, as shown in

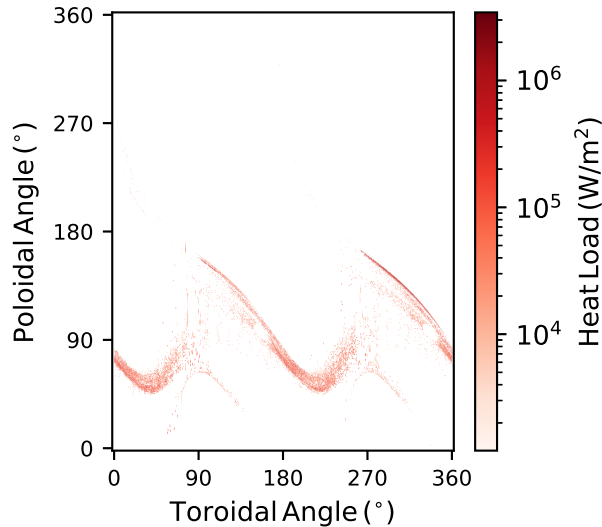


Figure 15. Lost deuteron heat load to the first wall of Eos.

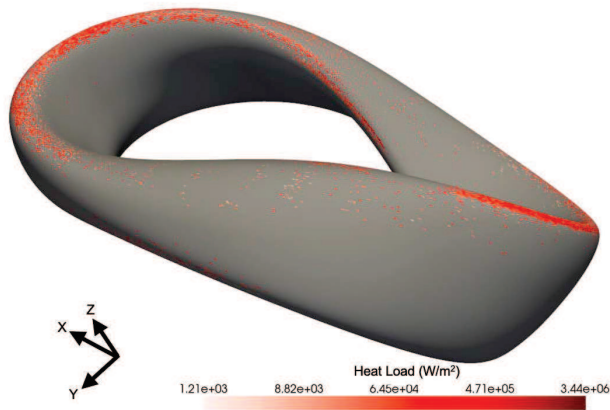


Figure 16. Lost deuteron heat load to the first wall of Eos.

Figure 3, was constructed from a tri-mesh grid such that losses in 3D-space could be recorded and a heat flux calculated. The maximum heat load is  $3.44 \pm 0.2$  MW/m<sup>2</sup>. The loss pattern is very non-uniform and is strongest on the top-half of the machine due to upward drifts. This loss pattern can be localized to the bottom-half of the machine if it were designed with the opposite helicity or the direction of the magnetic field were reversed. The losses in 3D-space are displayed in Figure 16 where the loss deposition on the top-half of the machine along regions of poor curvature is readily apparent. 3.5 MW/m<sup>2</sup> heat losses are tolerable and similar to what W7-X has observed [44]. Future work, however, should consider transient events which could enhance these localized losses to intolerable levels.

#### 4.1. Neutron Production

The ASCOT5 code contains a fusion source integrator [33] that calculates the fusion products based on the supplied reactants. In this case, the reactants are the deuterium NBI ions and the thermal deuterons, which will produce beam-thermal, beam-

beam, and thermonuclear reactions. The fusion source integrator iterates over each cell in the distribution functions and creates fusion products via Monte-Carlo sampling. A pair of markers is sampled from the reactant distributions, and the velocities of the fusion products for a given reaction are calculated using the initial velocities. The reaction probability, which depends on the relative velocity between the reactants, is used to weight the products which in turn are used to calculate the output fusion product distribution.

The same thermal profiles as shown in Figure 2 were used as input to the fusion source integrator, where the velocity distributions were treated as Maxwellian. The slowed NBI distribution, shown in Figure 10 (c), was used for the steady-state beam distribution. Since Eos will function as a fusion neutron source, only the  $D + D \rightarrow He^3(0.82MeV) + n(2.45MeV)$  reaction was considered.

The fusion source integrator was ran with 1000 Monte-Carlo markers per cell for beam-thermal, beam-beam, and thermonuclear reactions, calculating the DD-neutron source. The total neutron source rate was found to be  $2.5 \times 10^{17} \pm 2.5 \times 10^{16}$  neutrons/s. It has been shown that the dominant error source in the fusion source integrator stems from the reactant profiles [33, 45]. Since the thermal profiles have been artificially constructed for the equilibria with no error bars, a 10% uncertainty has been taken to mimic experimental measurement error. Beam-thermal interactions accounted for 79% of all neutrons produced, while 21% of neutrons were produced from thermal reactions. Beam-beam reactions are negligibly small. The Monte-Carlo ASCOT neutron source calculations are in good agreement with additional 1D plasma modeling of an Eos facility [27].

#### 4.2. DD-Triton Confinement

The confinement of DD-born tritons is also of interest in Eos. If tritons are sufficiently confined, then they may fuse and produce further neutrons. Therefore, the fusion source integrator was also used to consider the  $D + D \rightarrow T(1.01MeV) + p(3.02MeV)$  interaction to obtain the fusion triton source distribution. While the triton confinement can be examined, ASCOT5 cannot calculate the likelihood of a secondary fusion event as a function of time. Rather, the fusion source integrator would need to be used again with the supplied triton distribution. This is not fully self-consistent as the triton distribution evolves and slows, so, for now, only the overall triton confinement will be assessed.

The confinement properties and physics of the DD-born tritons are similar to that of the DT-born alphas in the following section, so the bulk of the discussion will follow. In short, the tritons have two main loss regimes: prompt losses and continuously

slowed losses. For 100,000 markers,  $66.1\% \pm 2.6\%$  tritons were lost, of which  $37.2\% \pm 1.9\%$  were prompt losses and  $9.4\% \pm 1.0\%$  were sufficiently slowed prior to lost. Therefore, about 34% of the tritons are fully confined with an additional 9.4% which slowed prior to being lost, meaning a conservative 43.4% could produce secondary fusion events. It should be noted, however, that TFTR experiments measured DD-triton burnup at less than 1% [46], and Eos tritons will be more susceptible to quasisymmetry induced losses. Therefore, only a minor fraction of the approximately 40% confined tritons are expected to undergo a secondary fusion event. A more thorough examination of the DD-triton burnup should be done in the future, but it is presumed to have only a small impact on the total neutron production and plasma heating.

#### 4.3. Hot-Electron Plasma

1D plasma modeling by Thea Energy has also shown that a hotter, less dense plasma may be more advantageous for tritium production in Eos [27]. As such, this scenario is briefly discussed here. The Eos equilibrium was kept constant while the thermal profiles in Figure 17 were supplied. While

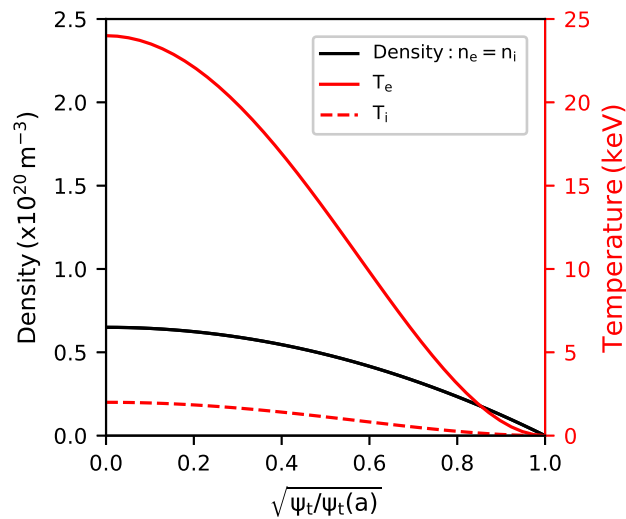


**Figure 17.** Thermal profiles for a hot-electron plasma with low density.

this is no longer self-consistent with the equilibrium, effects from alterations in the beam deposition and collisionality can still be examined. Most notably, the thermal profiles in Figure 17 portray a high electron temperature that is strongly peaked on-axis.

10,000 test particles were examined with all collisions included as an initial analysis to save on compute time due to the longer slowing down. Figure 18 presents some key features of the beam ions lost to the wall. Subplot (a) displays a histogram of the losses as a function of time. Notably, the prompt losses have been substantially reduced to about 1%. The lower plasma density allows for more core-localized beam

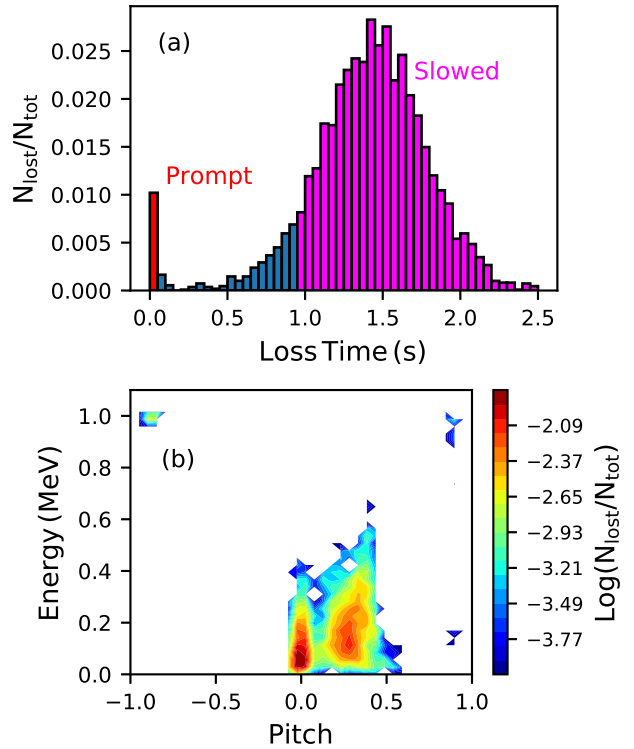


**Figure 18.** Beam losses in the hot-electron plasma as a function of time, (a), and energy-pitch, (b). The same color labeling of prompt losses (red) and slowed losses (magenta) still applies.

deposition, reducing the number of markers born near the plasma periphery which are quickly lost. The region of losses that have slowed, or near-slowed, has also been enhanced. This is visible in the time-histogram in subplot (a) and the energy-pitch histogram in subplot (b). Within energy-pitch space, the weak prompt losses are still visible at 1 MeV at pitch  $\pm 1$ , but the only other loss feature exists near low pitch and sub 400 keV.

The above results are rather advantageous. The prompt losses have been drastically reduced and high energy losses are minimal while low energy losses dominate. Lower energy losses translate to a reduced first wall heat flux and improved plasma heating efficiency. For reference, the particle loss fraction, after discarding sufficiently slowed ions, is  $9.7\% \pm 3.1\%$  and the energy loss fraction is  $4.0\% \pm 1.0\%$ . (See Tables 1 and 2 in the conclusion for comparison to the standard Eos scenario). While this is only an initial analysis, it is apparent that an equilibrium with a high electron temperature and low density presents substantial benefits from a fast ion perspective and may be considered for future scenario development.

## 5. Alpha Confinement in an Enlarged Eos

Thea Energy plans to construct a fusion pilot plant that will operate DT-plasmas with no NBI for external heating. Therefore, the alpha particles produced from DT-fusion [ $D + T \rightarrow He^4(3.52MeV) + n(14.06MeV)$ ] will be fully created from thermonuclear

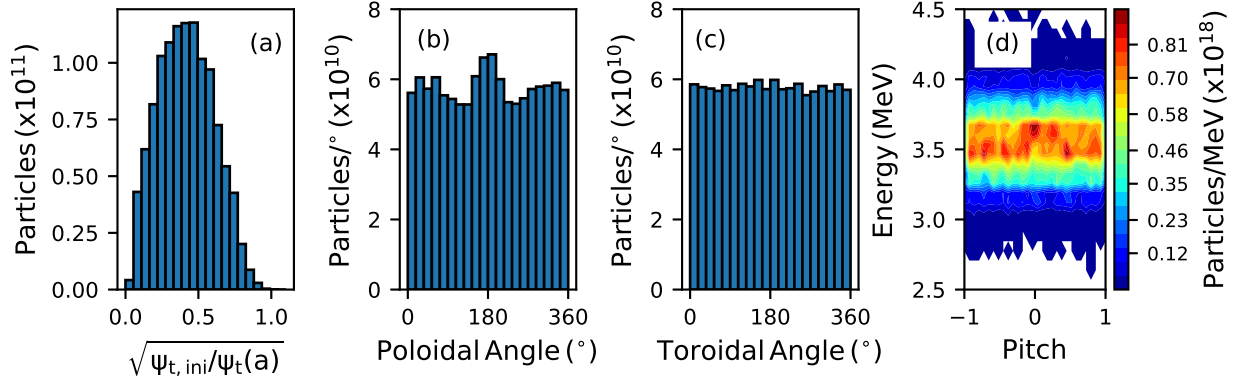


**Figure 19.** DT-alpha initial distribution as a function of root-normalized toroidal flux, (a), poloidal angle, (b), toroidal angle, (c), and (energy,pitch)-space, (d).

reactions. We consider a geometric rescaling of the Eos equilibrium by a factor of 2 with a DT-plasma as a preliminary testbed. The thermal profiles are the same with a peak temperature and density of  $2 \times 10^{20} \text{ m}^{-3}$  and 8 keV, respectively. 8 keV is likely lower than the optimal operating temperature of a DT fusion pilot plant but is used in this analysis for specificity and comparison to other models.

The ASCOT fusion source integrator was again used to calculate the alpha source profile. The total fusion source rate was found to be  $1.95 \times 10^{20}$  alphas/s. The initial distribution is shown in Figure 19. The distribution is isotropic in pitch-space with a birth energy around 3.5 MeV, and the number of particles per rho bin is peaked near  $\sqrt{\psi_p/\psi_p(a)}=0.2$  (particles per volume is peaked on axis).

100,000 markers were sampled from this distribution for analysis and particle tracing. Again, all collisions were included unless specified, and the markers were treated in a guiding-center fashion until they reached  $\sqrt{\psi_p/\psi_p(a)}=0.8$  at which point the full orbit motion was calculated. The loss fraction as a function of time is plotted in Figure 20. Near  $t=0$ , a large num-

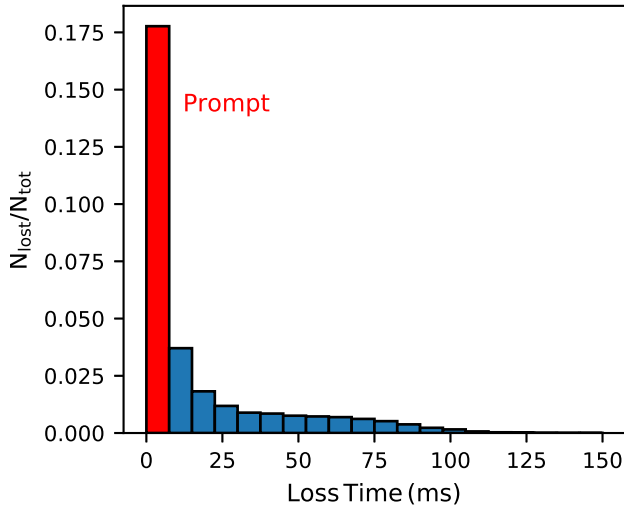


**Figure 20.** Alpha loss fraction as a function of time. The red bar denotes the region of dominant prompt losses.

ber of prompt losses are observed. The total loss fraction is  $30.4\% \pm 1.7\%$ . This is not unexpected as some alpha particles are born near the plasma edge. Furthermore, the large initial energy of 3.5 MeV allows for more rapid, immediate, losses. Ignoring the prompt losses, the loss fraction becomes  $12.9\% \pm 1.1\%$ . Ideally, the loss fraction would be lower, which motivates a new equilibrium with optimization including a metric for fast particle confinement.

For reference, a 3.5 MeV alpha particle in the presented plasma will experience a slowing-down time of about 70 ms. The slowing-down trend can again be observed as a function of energy in Figure 21, where the dashed line in subplot (a) is the theoretical energy decay for a 3.5 MeV alpha particle with a slowing-down time of 67 ms. The simulation was repeated with all collisions, only energy slowing, and no collisions. Compared to the beam ions in Eos, there is a much more gradual accumulation of losses. Instead of having two distinct loss populations (prompt and slowed), the alpha particles are strongly prompt lost followed by a continuous loss until thermalization. Please note the log scale in Figure 21; the slowing particles are lost at an ever decreasing rate.

Unlike the beam particles in Eos, the collisional effects of alphas is reduced and does not strongly alter the losses. Only a minor change is observed between subplots (a) and (b). This infers that orbital drift effects are the dominating loss mechanism. This is further reinforced from subplot (c) which shows continual alpha losses up until the simulation end time (500 ms) in the absence of all collisions.

Figure 22 examines the initial radius of the lost alphas. Again, the results largely differ from the beam-born ions in Eos shown in Figure 13. The prompt losses near  $t=0$  now extend much deeper into the core of the plasma. Secondly, the smooth and continuous presence of losses is present at all radii. Lastly, strong core losses are observed regardless of the presence of collisions. It appears that the higher energy alpha

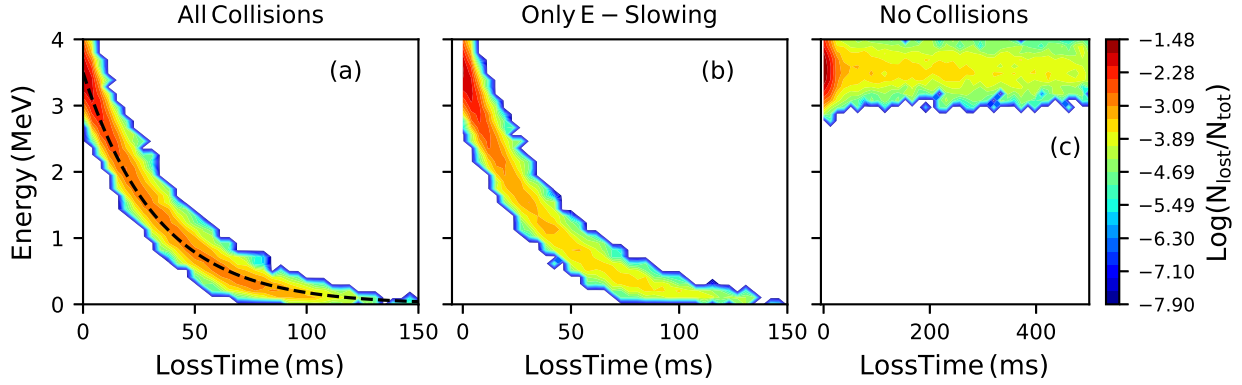


**Figure 21.** Alpha born loss fraction as a function of time and particle energy for simulations including all forms of collisions, (a), only energy slowing collisions, (b), and no collisions, (c). The dashed black line in (a) is the exponential energy decay from theory for a 3.5 MeV alpha particle with a slowing time of 67 ms.

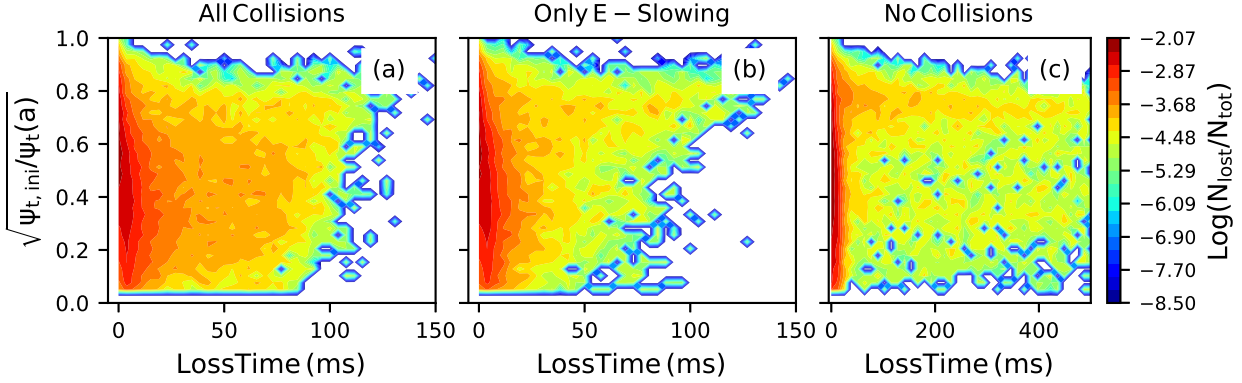


**Figure 22.** Alpha born loss fraction as a function of time and initial root-normalized toroidal flux for simulations including all forms of collisions, (a), only energy slowing collisions, (b), and no collisions, (c).

particles succumb to drift effects much sooner than the 1 MeV beam ions. Subplots (c) reveal that regardless of alpha initial position and given sufficient time, the alphas will become lost. This is indicative of non-zero drift motion which will slowly push the alphas outward irrespective of location.

The total alpha energy loss accounts for  $22.4\% \pm 1.5\%$  of the initial alpha energy. While early losses still dominate and are close to the birth energy, slowed losses bring the lost energy fraction down from the lost particle fraction of 30.4%. The wall heat load calculated from the lost alphas is shown in Figures 23 and 24. The peak heat load is  $7.71 \pm 0.2$  MW/m<sup>2</sup>. A similar loss pattern to Figure 15 is observed except the overall heat flux is higher due to the larger alpha energy. The calculated heat loads are below the tolerable allowances for most first wall materials in a reactor [47, 48], but future work should consider transient or MHD events which could drive localized losses and hot spots.

## 6. Conclusion and Discussion

This paper examines the confinement and transport of energetic particles in Thea Energy’s stellarator designs. In particular, Thea Energy plans to produce a neutron-source machine with NBI (Eos) and

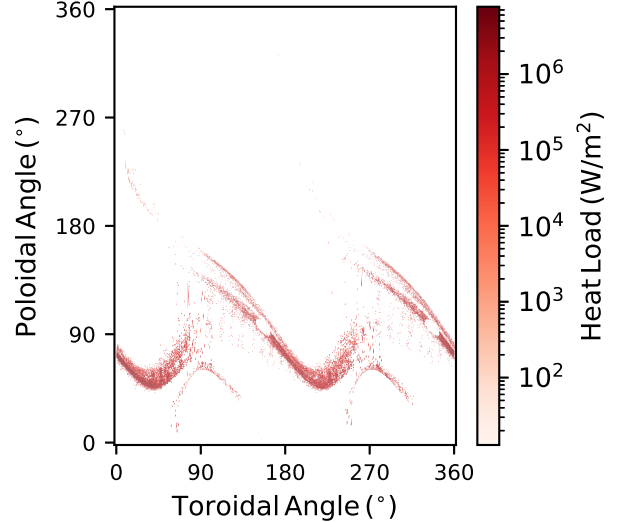


**Figure 23.** Lost alpha heat load to the first wall of the doubly-scaled Eos.

a DT-fueled fusion pilot plant (Helios). They are employing a quasi-axisymmetric geometry with two-fold periodicity. The equilibria exhibit the typical confinement properties of fast ions in optimized stellarators: good overall core confinement, enhanced confinement of trapped orbits, and a loss-cone structure that strongly impacts low pitch ions. Prompt losses dominate in all cases when ions are born near the plasma

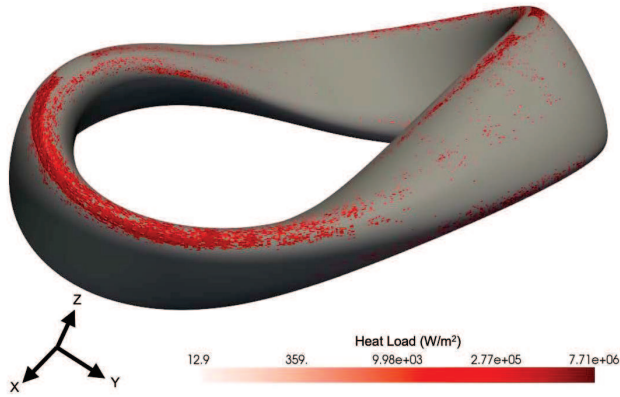


**Figure 24.** Lost alpha heat load to the first wall of the doubly-scaled Eos.

edge, but core confinement (inward of  $\sqrt{\psi_t/\psi_t(a)}=0.6$ ) is generally good. Collisions appear to have a larger impact on the confinement of NBI ions compared to alpha particles in Eos-like equilibria.

Table 1 summarizes the fraction of lost ions (%) for different scenarios in Eos, the doubly-scaled Eos, and the standard Eos case with a hot, tenuously peaked, electron temperature (Section 4.3) for their respective beam ion and alpha populations. The table shows the losses when considering only the equilibrium (i.e. without collisions), the equilibrium with collisions, and with collisions but ignoring fast ions that have been sufficiently thermalized. Prompt losses are included. The equilibrium only case was not calculated for the hot Eos case. Likewise, Table 2 presents the energy loss

**Table 1.** Particle loss percentage (%) of lost beam-born particles in Eos and hot tenuously peaked Eos and alpha particles in the enlarged Eos for 3 scenarios: equilibrium only, equilibrium with collisions, and with the removal of near-thermalized losses.

	Equ. Only	w/ Colls	No Therms
Eos	12.0	22.1	10.4
2x Eos DT	25.8	30.4	29.8
Eos HTP	N/A	44.5	9.8

fraction (%) for the same scenarios. It is noted that the particle loss fraction is the same as the energy loss fraction for the equilibrium only cases because energy is conserved. In general, the energy loss fractions are lower as some particles have partially slowed via collisions.

**Table 2.** Energy loss percentage (%) of lost beam-born particles in Eos and hot tenuously peaked Eos and alpha particles in the enlarged Eos for 3 scenarios: equilibrium only, equilibrium with collisions, and with the removal of near-thermalized losses.

	Equ. Only	w/ Colls	No Therms
Eos	12.0	8.5	7.4
2x Eos DT	25.8	22.4	22.4
Eos HTP	N/A	8.1	4.0

In short, the confinement of beam ions in Eos is quite good. The modeling shows 10% of losses

after discarding slowed beam ions, and can produce on order of  $2 \times 10^{17}$  neutrons/s. From an initial fast ion perspective, the feasibility of the Eos neutron-source design appears viable. In regards to alpha confinement, however, a slightly higher alpha loss particle fraction around 30% is observed, which motivates the construction of a new equilibrium and a successive optimization including a metric for fast ion confinement. This is in large part due to the higher alpha energy which produces larger orbit drifts and greater outward transport. For this study, the only difference among the two magnetic topologies is a geometric scaling. Thus, one would expect higher losses for higher energy ions within the same equilibria. With a possible increase in field strength and/or rotational transform, one would expect a reduction in the alpha losses. Prior studies have shown that higher rotational transforms in quasi-axisymmetric configurations reduce orbit widths which in turn reduces fast ion losses [49, 25].

The final analysis poses the question of tolerability. Using the ISS04 scaling for energy confinement time [50] as was done in [27], one can find that the heating power scales as  $P^{-0.61}$ . Using the same approach as in [51] and [52] for ITER, one can assume a 10% margin of error in the energy confinement to achieve ignition. Following this methodology, one can find that the lower bound of this limit would incur for 25% alpha losses. The current equilibrium is just sufficient with respect to this threshold with room for improvement.

The much more stringent condition is the allowable heat flux to plasma facing components. The analysis performed in the manuscript shows that the calculated wall heat loads are similar to current experiments and, while very high, should be tolerable with careful design. However, additional MHD transport, or other anomalous loss mechanisms, need to be included in the analysis. Even a few percent of alpha losses over time may induce impurity sputtering and accumulation which will degrade plasma performance [52, 53]. Thus, future designs should aim for much lower alpha losses than is currently simulated and reperform the analysis for localized, ‘hot-spot,’ losses.

This paper quantitatively verifies the fast ion confinement properties within quasi-axisymmetric equilibria due to guiding-center and full-orbit drifts and collisions. This is in regards to equilibria which have been optimized without any constraints on the fast ion confinement. Analysis is presented on thermal profile construction, neutron sourcing, and wall heat loads. In conclusion, the fast ion confinement properties of Thea Energy’s Eos concept equilibrium seem tolerable and do not pose any major concerns towards future plans. It is suggested that the

equilibrium optimization include a metric for fast ion confinement to improve the results with respect to DT-born alphas. While this paper only reports on the initial confinement properties, additional energetic particle effects need to be considered in future analysis. A large concern for all stellarators is the impact of MHD instabilities, namely Alfvén eigenmodes and other fast ion driven modes [54], on energetic particle confinement. Additionally, for substantial fast ion populations, such as large NBI heating or burning plasmas, the presence of fast ion currents and pressures should be kinetically included in the equilibria. This may produce MHD and island structures which in turn could alter the fast ion confinement itself. These are larger areas of study and active research, but pose open questions for the creation of quasi-axisymmetric equilibria and Thea Energy’s future work.

### Acknowledgements

This work was supported by the U.S. Department of Energy under contract number DE-AC02-09CH11466. The United States Government retains a non-exclusive, paid-up, irrevocable, world-wide license to publish or reproduce the published form of this manuscript, or allow others to do so, for United States Government purposes. This award was funded by an INFUSE Award given in round 2022b.

### References

- [1] Brevnov N and Tomashchuk Y 1964 *Nucl. Energy, Part C Plasma Phys.* **6** 161
- [2] Egedal J *et al.* 2022 *Nucl. Fusion.* **62** 126053
- [3] Heidbrink W, Sadler G *et al.* 1994 *Nucl. Fusion* **34** 535
- [4] White R *et al.* 1996 *Pphys. Plasmas* **3** 3043
- [5] Spong D 2011 *Phys. Plasmas* **18** 056109
- [6] Mynick H 2006 *Phys. Plasmas* **13** 05812
- [7] Landreman M and Catto P 2006 *Plasma Phys. Control. Fusion* **53** 015004
- [8] Landreman M and Catto P 2006 *Phys. Plasmas* **19** 056103
- [9] Boozer A 1981 *Phys. Fluids* **24** 1999
- [10] Landreman M and Paul E 2022 *Phys. Rev. Lett.* **128** 035001
- [11] Mynick H, Chu T and Boozer A 1982 *Phys. Rev. Lett.* **48** 322
- [12] Cary J and Shasharina S 1997 *Phys. Plasmas* **4** 3323
- [13] Cary J and Shasharina S 1997 *Phys. Rev. Lett.* **78** 674
- [14] Canik J 2007 *Phys. Rev. Lett.* **98** 085002
- [15] Canik J 2007 *Phys. Plasmas* **14** 056107
- [16] Pedersen T 2022 *Nucl. Fusion* **62** 042022
- [17] Beidler C *et al.* 2021 *Nature* **596** 221
- [18] LeViness A *et al.* 2023 *Nucl. Fusion* **63** 016018
- [19] Rodriguez E *et al.* 2020 *Phys. Plasmas* **27** 062501
- [20] Nemov V *et al.* 2005 *Phys. Plasmas* **12** 112507
- [21] Bader A *et al.* 2021 *Nucl. Fusion* **61** 116060
- [22] Velasco J 2021 *Nucl. Fusion* **61** 116059
- [23] Bindel D *et al.* 2023 *Plasma Phys. Control. Fusion* **65** 065012
- [24] Bader A *et al.* 2019 *J. Plasma Phys.* **85** 905850508
- [25] Paul E *et al.* 2022 *Nucl. Fusion* **62** 126054
- [26] Kruger T, Martin M *et al.* 2024 *Nucl. Fusion* “The planar coil stellarator: coil optimization methods” Submitted
- [27] Swanson C *et al.* 2024 *Nucl. Fusion* “Plasma physics models for the early-stage design and optimization of eos: a sub-breakeven, deuterium-deuterium, beam-target fusion, stellarator neutron source facility” Accepted
- [28] Hemsworth R *et al.* 2017 *Nucl. Fusion* **19** 025005
- [29] Varje J, Sarkimaki K, Kontula J, Ollus P, Kurki-Suonio T, Snicker A, Hirvijoki E and Akaslompolo S “High-performance orbit-following code ascot5 for monte carlo simulations in fusion plasmas.” arXiv preprint arXiv:1908.02482, 2019.
- [30] Akaslompolo S *et al.* 2019 *JINST* **14** C10012
- [31] Mulas S *et al.* 2022 *Nucl. Fusion* **62** 106008
- [32] McMillan M and Lazerson S 2014 *Plasma Phys. Control. Fusion* **56** 095019
- [33] Siren P *et al.* 2018 *Nucl. Fusion* **58** 016023
- [34] Reiman A *et al.* 1999 *Plasma Phys. Control. Fusion* **41** B273
- [35] Reiman A *et al.* 1999 *Phys. Plasmas* **8** 2083
- [36] Landreman M, Buller S and Drevlak M 2022 *Phys. Plasmas* **29** 082501
- [37] Dudt D *et al.* 2023 *J. Plasma Phys.* **89** 955890201
- [38] Dudt D and Kolemen E 2020 *Phys. Plasmas* **27** 102513
- [39] Rodriguez E *et al.* 2022 *J. Plasma Phys.* **88** 90588010
- [40] Redl A *et al.* 2021 *Phys. Plasmas* **28** 022502
- [41] Shu C 2020 *Nucl. Fusion* **60** 089601
- [42] Guasp J and Liniers M 2000 *Nucl. Fusion.* **40** 397
- [43] Moseev D and Salewski M 2019 *Phys. Plasmas* **26** 020901
- [44] Wurden G 2017 *Nucl. Fusion* **57** 056036
- [45] Siren P *et al.* 2019 *Fusion Eng. Des.* **146** 1587
- [46] Hendel H and Sadler D 1990 *Nucl. Sci. Eng.* **106** 114
- [47] Linke J *et al.* 2019 *Matter Radiat. Extremes* **4** 056201
- [48] Lazerson S *et al.* 2021 *Plasma Phys. Control. Fusion* **63** 125033
- [49] Buller S, Landreman M, Kappel J and Gaur R “A family of quasi-axisymmetric stellarators with varied rotational transform.” arXiv preprint arXiv:2401.09021, 2024.
- [50] Yamada H *et al.* 2005 *Nucl. Fusion* **45** 1684
- [51] Putvinski S 1998 *Nucl. Fusion* **38** 1275
- [52] ITER Physics Expert Group on Energetic Particles, Heating and Current Drive and ITER Physics Basis Editors 1999 *Nucl. Fusion* **39** 2471
- [53] Bonfiglio P *et al.* 2024 *Nucl. Fusion.* **64** 096038
- [54] Paul E *et al.* 2023 *J. Plasma Phys.* **89** 905890515